SCIENTIFIC REPORTS

OPEN

Brillouin spectroscopy of fluid inclusions proposed as a paleothermometer for subsurface rocks

Received: 30 September 2014
Accepted: 09 July 2015
Published: 28 August 2015

Mouna El Mekki-Azouzi[1], Chandra Shekhar Pati Tripathi[1], Gaël Pallares[1], Véronique Gardien[2] & Frédéric Caupin[1]

As widespread, continuous instrumental Earth surface air temperature records are available only for the last hundred fifty years, indirect reconstructions of past temperatures are obtained by analyzing "proxies". Fluid inclusions (FIs) present in virtually all rock minerals including exogenous rocks are routinely used to constrain formation temperature of crystals. The method relies on the presence of a vapour bubble in the FI. However, measurements are sometimes biased by surface tension effects. They are even impossible when the bubble is absent (monophasic FI) for kinetic or thermodynamic reasons. These limitations are common for surface or subsurface rocks. Here we use FIs in hydrothermal or geodic quartz crystals to demonstrate the potential of Brillouin spectroscopy in determining the formation temperature of monophasic FIs without the need for a bubble. Hence, this novel method offers a promising way to overcome the above limitations.

Various climate proxies have been used to estimate the variability of the surface air temperature prior to the existence of instrumental records[1]. They include global proxies, for instance the isotopic ratio between ^{18}O and ^{16}O in ice cores[2,3] or in shell of fossil marine organisms[4,5]; and local proxies, such as tree rings studies[6–8], palynological studies[9], and fluid inclusions (FIs)[10–12]. FIs are present in virtually all rocks on Earth. A record of the fluid chemistry and environment at the time of rock formation can be kept in FIs for billions of years[13]. FIs are thus considered to be direct samples of the volatile phases which circulated through the Lithosphere over the course of the Earth's history. From their study some general rules have emerged, which have led e.g. to a model of fluid distribution in the earth's crust and upper mantle[14–16] or to the reconstruction of the composition of sea-water through time[17–21]. FIs are among the most useful witnesses of many natural processes on Earth in which fluids play a role.

FIs are small cavities (with a typical size from 1 to 100 μm) in minerals. The usual assumption about the path followed in the pressure-temperature plane by the liquid in a FI is schematically illustrated on Fig. 1a. We are interested in FIs that were initially filled with a homogeneous fluid during their formation in the host mineral at the formation temperature T_f and pressure P_f (point A in Fig. 1a). If cooled, the monophasic FI follows a curve (ABCD) that crosses the liquid-vapour equilibrium curve at a temperature T_X (point B). Upon further cooling, the liquid often becomes metastable (curve BCD) and, usually, a vapour bubble nucleates (transition from D to E). When a bubble bearing FI is heated in a micro-thermometric study (curve EFB), the bubble shrinks and eventually disappears at the homogenization temperature T_h (point B). Here $T_h = T_X$. For a rigid host mineral, the density of the liquid along AB is constant. Hence, the isochore starting at T_X from the liquid-vapour equilibrium curve is used as the locus of possible formation temperatures (and corresponding pressures)[22]. To determine T_f,

[1]Institut Lumière Matière, UMR5306 Université Claude Bernard Lyon 1-CNRS, Université de Lyon and Institut Universitaire de France, 69622 Villeurbanne Cedex, France. [2]UMR CNRS 5276 Laboratoire de Géologie de Lyon, Université Lyon1/ENS Lyon, Campus de la Doua, 2 rue Raphaël Dubois, 69622 Villeurbanne Cedex, France. Correspondence and requests for materials should be addressed to F.C. (email: frederic.caupin@univ-lyon1.fr)

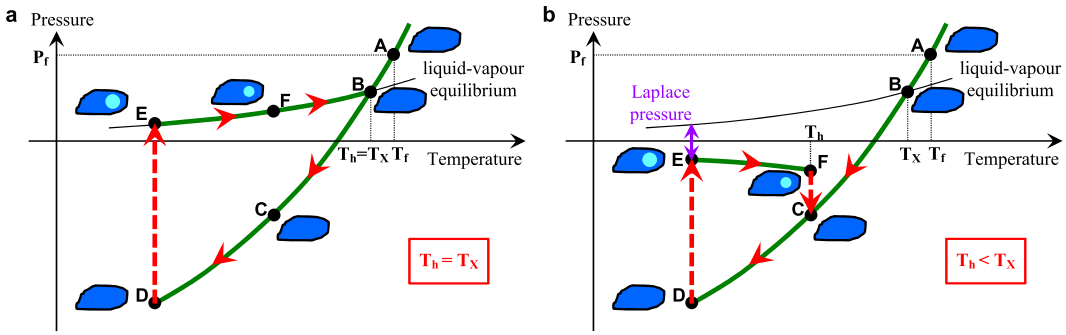

Figure 1. Schematic path followed by fluid inclusions (FIs). Note that the axis are not to scale. (**a**) Commonly assumed path. A monophasic FI is formed at a temperature T_f and pressure P_f (A). During cooling, the pressure of the liquid is reduced along an isochore (curve AB) and the liquid becomes metastable with respect to the vapour phase (curve BCD). This may lead to nucleation of a vapour bubble (transition from D to E), producing a biphasic FI (E). During heating, the FI follows the bulk liquid-vapour equilibrium (LVE) (curve EFB), the bubble shrinks, and eventually disappears at $T_h = T_X$ (B). This assumption is valid for FIs with low fluid density and large volume. (**b**) Path modified by surface tension effects. Surface tension and the associated Laplace pressure lead to LVE at pressures below the bulk LVE (path EF)[33]. Eventually the bubble collapses (transition from F to C) at a temperature T_h, bringing back the FI on the isochore (curve ABCD). Surface tension thus causes T_h to be strictly less than T_X. This effect is relevant for FIs with high fluid density and small volume[33]. In contrast, warming the monophasic FI along the isochore and finding with Brillouin spectroscopy the crossing point B with the bulk LVE curve gives the correct T_X.

another piece of information is needed, such as the local geothermal gradient, which gives the relation between depth, pressure, and temperature. T_f then corresponds to the intersection of the isochore and the geothermal gradient curve. If the pressure is high, T_X can be much lower than T_f. But for rocks formed at atmospheric pressure, relevant for paleoclimate, one has $T_f = T_X$. If the equality $T_h = T_X$ holds, the bubble disappearance temperature T_h would thus provide the temperature T_f prevailing during the mineral formation.

However, the use of T_h for this purpose suffers from two important limitations. The first is simply the absence of bubble; this situation can be due to a weak metastability (i.e. high energy barrier for bubble nucleation and low nucleation rate) that is not sufficient to lead to bubble nucleation. Previous research has concentrated in developing methods to artificially stimulate bubble nucleation[23–28]. The standard procedure consists in cooling the samples below −10 or −20 °C for several days or even weeks[10,25,29]. But there are fundamental limitations with this method such as the potential stretching of the inclusion and its neck-down during repeated cycles of cooling/heating[30,31]. A more recent technique consists in focusing femtosecond laser pulses to overcome metastable states at room temperature[32]. In this case the threshold laser intensity must be controlled because it can damage the mineral, and thus change the volume of the inclusion, or cause leakage or stretching[11]. The above mentioned methods may work if the bubble is absent for kinetic reasons, that is when the bubble does not appear spontaneously in an observable time without stimulation because the nucleation rate in the metastable liquid is too low. However, the bubble can also be absent for thermodynamic reasons, when the free energy of the biphasic FI is always *higher* than that of the monophasic FI. This situation, due to surface tension effects[33,34], occurs for FIs small in size and which contain a fluid at high density. Even if a bubble was created in such a system, it would disappear immediately and the FI would become monophasic again. Even for FIs in which the state with bubble (naturally present or nucleated by one of the above means) can be thermodynamically stable, a second limitation is a possible bias when assuming $T_h = T_X$. Because of the small radius of curvature of the bubble, surface tension induces a Laplace pressure difference between the liquid and vapour phase, which modifies the liquid-vapour equilibrium (Fig. 1b). The bubble collapse (transition from F to C) then occurs at $T_h < T_X$. A correction based on a detailed thermodynamic model has been derived[33]. However, as the model requires an accurate formulation for the free energy of the fluid, it was applied only to the case of pure water, for which an accurate equation of state is available. Further sources of uncertainty arise from the need to measure the bubble radius, and from the fact that the state with bubble remains metastable in a range of temperatures. All these effects make T_h lower than the actual T_X, with a larger shift (up to several degrees) for smaller inclusions and/or denser liquids.

We propose to overcome the above limitations using Brillouin spectroscopy to directly determine T_X without the need for a bubble and its T_h. Brillouin scattering from a liquid results from the inelastic interaction of light with the thermal density fluctuations (acoustic waves) of the liquid[35]. The frequency of the scattered light is shifted from that of the incoming light by an amount Δf_B proportional to the sound velocity in the liquid. Δf_B thus depends on the liquid, its temperature and density. For the liquid

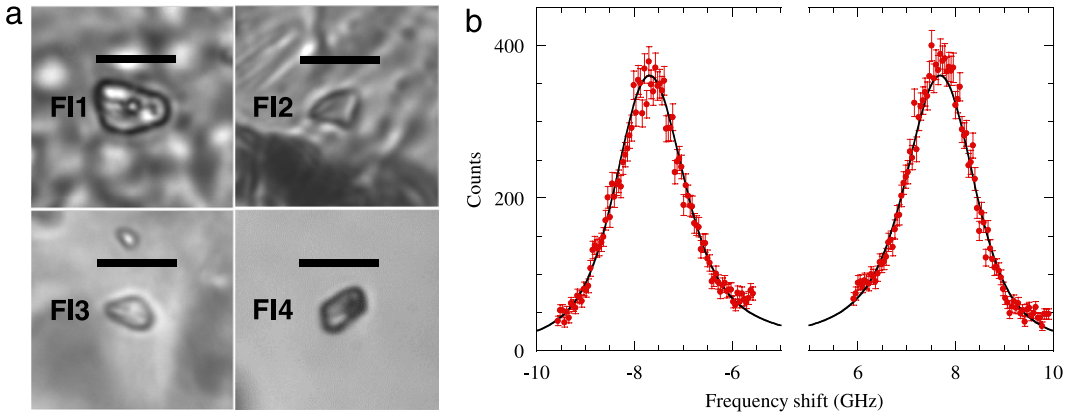

Figure 2. Fluid inclusions studied in this work. (**a**) Microphotographs of FIs used in this study (scale bars: 7 μm): one synthetic (FI1) and two natural (FI2 and FI3) FIs containing pure water, and one natural FI (FI4) containing dissolved salts. (**b**) Example of Brillouin spectrum (here recorded for FI3 at 50 °C). Error bars show the shotnoise equal to the square root of the counts. The red curve is a fit with equation (1), which yields the value of $\Delta f_B = 7.746$ GHz for this example.

along its liquid-vapour equilibrium (LVE), the Brillouin shift as a function of temperature $\Delta f_B^{LVE}(T)$ is known from calculations, or calibration measurements (see Methods). Now, when a monophasic FI is warmed or cooled, the liquid that it contains does not follow the LVE, but an isochore (see Fig. 1). Δf_B along an isochore at density ρ is a function of T uniquely determined by ρ. Therefore, measuring $\Delta f_B(T)$ for the monophasic FI defines a curve that, by definition, crosses $\Delta f_B^{LVE}(T)$ at T_X (see Fig. 1). Brillouin spectroscopy thus provides a non-destructive method to directly measure T_X in monophasic FIs containing pure or salty water, without the need to nucleate a bubble. Hence it is not biased by surface tension effects.

The aim of this paper is to provide a proof of concept of the method by measuring T_X on samples in which T_h can also be measured, and such that the assumption $T_h = T_X$ is valid. To this end, we have selected 4 FIs in quartz crystals (see Fig. 2a). Because these FIs where formed at a pressure P_f above atmospheric pressure, they are not directly relevant to paleoclimatic reconstruction. Yet their T_X are well defined and can be obtained based on the measured Brillouin shifts. Moreover, because the quartz host is robust, a bubble can be nucleated in the FIs by cooling-heating cycles, without damaging the crystal nor changing the FI volume. The T_h of each FI can then be measured by traditional microthermometry. For the fluid density and volume of the selected FIs, surface tension effects are negligible[33] and $T_h = T_X$. Therefore the comparison between measured T_h and T_X provides a benchmark for the proposed method.

Results

FIs containing pure water. Three samples (FI1, FI2 and FI3, see Fig. 2a) were chosen among those for which it is possible to nucleate a bubble by cooling-heating cycles. The 3 FIs contained pure water, based on their melting points with a bubble present. A typical Brillouin spectrum is shown on Fig. 2b (see Methods for more details). $\Delta f_B(T)$ was measured for each monophasic sample, leading essentially to a straight line (Fig. 3a). Two procedures were used to determine the temperature T_X at which $\Delta f_B(T)$ intersects the calculated LVE curve $\Delta f_B^{LVE}(T)$ (see Methods). The first one used the full $\Delta f_B(T)$ expression as a function of ρ based on formulations from the International Association for the Properties of Water and Steam (IAPWS) (see Methods). T_X was deduced from a fit to the data with ρ as a free parameter (Fig. 3a). The second, simpler procedure, consists in fitting the difference $\left[\Delta f_B - \Delta f_B^{LVE}(T)\right]$ to a straight line and find where it crosses zero (Fig. 3b). Table 1 shows that this second procedure agrees perfectly with the first one, while being simpler to implement.

FIs containing salty water. Next we turn to the more general case of a FI containing an aqueous solution. As an example, we have chosen a FI from the Mont-Blanc (FI4, see Fig. 2a). For this location, the most abundant anion is by far chlorine, and the dominant cation is Na^+ (around 80% in molality), as determined by several techniques[36]. Therefore, to calculate the reference Brillouin shift Δf_B^{LVE}, we have used data for pure NaCl solutions (see Methods). To obtain the total Cl^- molality, we used Raman spectroscopy[37] (see Methods). Molality is defined as the number of moles of Cl^- per kilogram of water in the solution. We find it better to work with *molality* rather than *molarity* (number of moles of solute per volume of solution), because molality does not depend on temperature and pressure for a system of fixed mass such as a fluid inclusion. We checked that the Raman spectra at 20 °C were identical whether a bubble was present or not. We obtained a total Cl^- molality $m_{Raman} = 1.25 \pm 0.05$ mol kg^{-1}. For comparison, the spectra from pure water and a bulk solution of NaCl with $m = 1.25$ mol kg^{-1} are displayed on

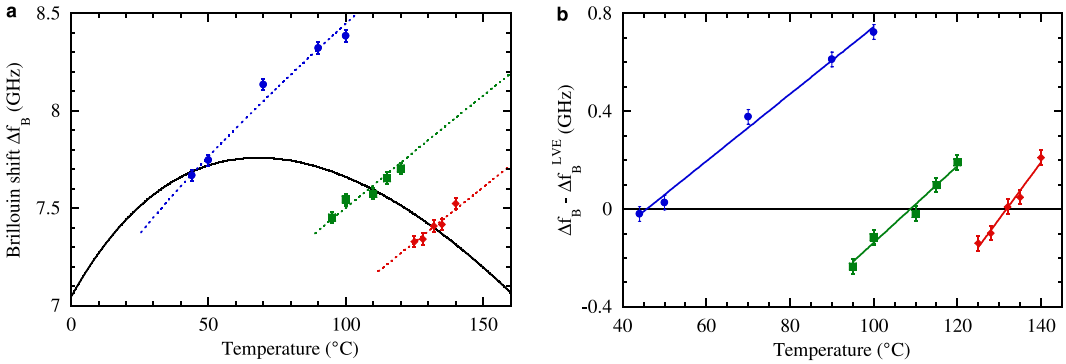

Figure 3. Determination of T_X with Brillouin spectroscopy for FIs containing pure water. (**a**) Brillouin shift Δf_B as a function of temperature for pure water. The solid black curve is Δf_B^{LVE} along the liquid vapour equilibrium. The data points show Δf_B for FI1 (red diamonds), FI2 (green squares), and FI3 (blue circles). The dotted curves show fits of the data with $\Delta f_B(T)$ calculated with formulations from the International Association for the Properties of Water and Steam (IAPWS) (see Methods), and treating the density ρ as a free parameter. The crossing point with the LVE curve gives for each FI T_X and its uncertainty (see Table 1). (**b**) The difference $\Delta f_B(T) - \Delta f_B^{LVE}$ is shown for each FI (same symbols as in panel (a)). A linear fit is performed on each data set (solid lines) to give T_X as the temperature at which it crosses zero, and its uncertainty (see Table 1).

Sample	visual T_h (°C)	T_X from Brillouin (°C)	
		fit IAPWS	linear fit of $\Delta f_B - \Delta f_B^{LVE}$
FI1	131.9 ± 0.5	131.8 ± 0.6	131.7 ± 0.6
FI2	107.9 ± 2	108.8 ± 0.7	108.8 ± 0.8
FI3	46.4 ± 0.4	45.4 ± 1.3	45.8 ± 1.5
FI4	120 ± 1	N.A.	120.5 ± 1.1

Table 1. Comparison of the T_h values obtain by direct observation of the bubble disappearance, with the T_X values obtained with the Brillouin method, using two types of fitting procedures. The error bars represent ± 1 standard deviation.

Fig. 4a: the latter spectrum is identical to the FI spectrum. As a further check, we also used Brillouin spectroscopy to measure the total Cl^- molality. First, we calculate the reference Brillouin curve $\Delta f_B^{LVE}(T, m)$ at temperature T and NaCl molality m from literature data (see Methods). We checked that our calculation agrees well with measurements on reference NaCl solutions (Fig. 4b). Then we took advantage of being able to nucleate a bubble in FI4. We measured Δf_B in the biphasic FI4 from 0 °C to T_h (Fig. 4c). We then treat m in $\Delta f_B^{LVE}(T, m)$ as a fitting parameter to reproduce the experimental values for Δf_B in the range 0–100 °C. The fit gives $m_{Brillouin} = 1.20 \pm 0.03$ mol kg^{-1}, in excellent agreement with m_{Raman}. This confirms the validity of our procedure. Moreover, Fig. 4c shows that our formula for $\Delta f_B^{LVE}(T, m)$ (see Methods) agrees with the FI data even outside the range of available measurements for the sound velocity. We now have all the ingredients needed to define a general procedure to determine T_X for a monophasic, salty FI. The total Cl^- molality m_{Raman} is measured by Raman spectroscopy and used to compute the reference Brillouin shift $\Delta f_B^{LVE}(T, m_{Raman})$. Then, the Brillouin shift $\Delta f_B(T)$ is measured on the monophasic FI. A linear fit to $\Delta f_B(T) - \Delta f_B^{LVE}(T, m_{Raman})$ gives T_X as the point where it crosses zero. We have shown above for pure water that this procedure was as accurate as using a full fitting of $\Delta f_B(T)$. The result for T_X for FI4 obtained in this way (Fig. 4c) matches well the T_h value obtained by direct observation of the bubble disappearance (see Table 1), thus validating the procedure for salty FIs.

The details of the above procedure are valid for FIs containing NaCl solutions. Different dissolved salts affect the properties of the solution in different ways. However, these differences remain small for Raman[37], refractive index[38] and sound velocity[39], which are the ingredients needed to apply the procedure we propose. Therefore, the equations for NaCl solutions will provide a good approximation for other solutes. If a better accuracy is needed, the composition of salts in the FI must be known for the studied location, or determined. This can be done for example by measuring the eutectic point of the aqueous solution, by Raman analysis of the solution[37,40] and of frozen salt hydrates[41], or using other (destructive)

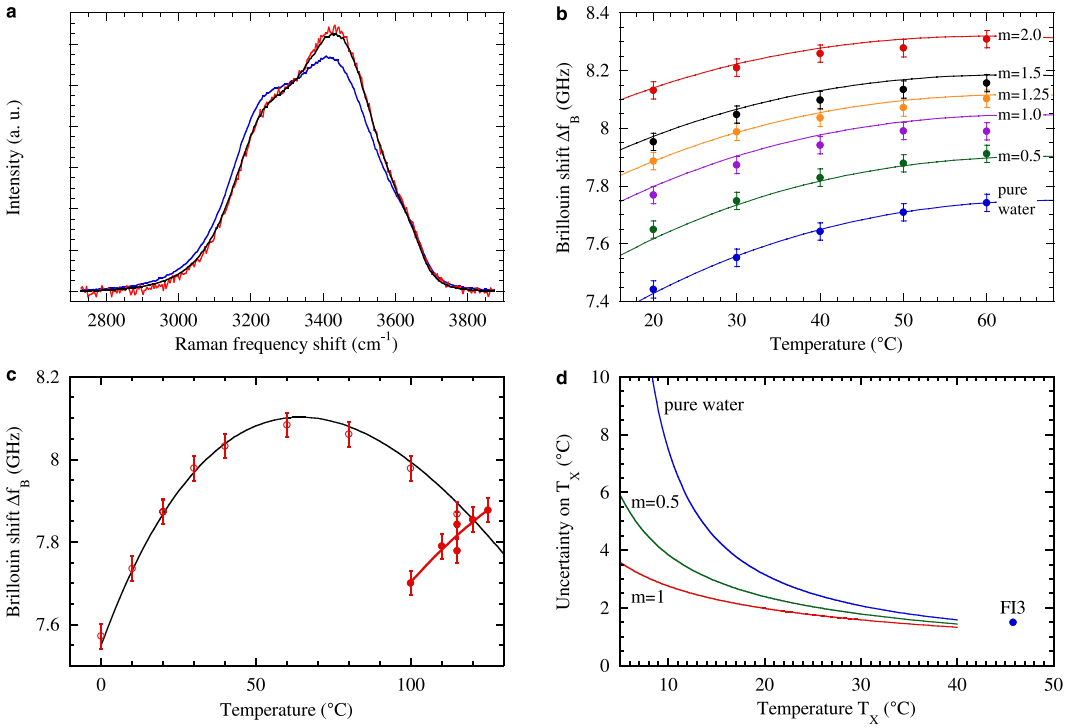

Figure 4. Determination of T_X with Brillouin spectroscopy for salt bearing FIs. (**a**) Comparison of Raman spectra at 20 °C (all normalized to unit area). The blue curve shows the OH stretching band of pure water. The spectrum from FI4 (red) exhibits a decrease at low shift and increase at high shift, typical of dissolved salt. A standard procedure[37] yields an equivalent NaCl molality $m_{Raman} = 1.25 \pm 0.05$ mol kg^{-1}. The spectrum from a bulk aqueous solution of 1.25 molal NaCl is also shown (black) for direct comparison. (**b**) Brillouin shift Δf_B as a function of temperature for reference NaCl solutions. The curves designated by the solution molality m (in mol kg^{-1}) were calculated from literature data (see Methods). They agree well with the corresponding experimental data (symbols). (**c**) $\Delta f_B(T)$ for FI4, with (open symbols) or without (closed symbols) bubble. The thin black curve is the calculated Δf_B^{LVE} for a NaCl solution with molality 1.20 mol kg^{-1}. The thick red curve is the result of the linear fitting procedure on $\Delta f_B(T) - \Delta f_B^{LVE}$; it intersects Δf_B^{LVE} at T_X. (**d**) Uncertainty δT_X (± 1 standard deviation) on T_X determined with Brillouin spectroscopy, as a function of T_X. The solid curves were calculated with equation (4) (see Methods) for pure water and NaCl solutions with designated molalities (in mol kg^{-1}). The marker shows the error on T_X from the linear fitting procedure for FI3, as given in Table 1.

techniques such as LIBS (laser-induced breakdown spectroscopy)[36] or LA-ICP-MS (laser-ablation inductively coupled plasma mass spectrometry)[42,43]. Then reference solutions can be prepared in the laboratory to record a series of Raman and Brillouin spectra for calibration, as was done in the present work for NaCl solutions. The reference Brillouin shift may also be calculated from refractive index and sound velocity data of the given solution if available (see Methods).

Uncertainty on T_X. The constant finite uncertainty on Δf_B translates into an increasing uncertainty on T_X at lower temperatures (Table 1). This is due to the fact that, whereas the slope of $\Delta f_B(T)$ along isochores remains nearly constant, the slope of $\Delta f_B^{LVE}(T)$ increases with decreasing temperature. For pure water, the two slopes eventually become equal at the temperature of maximum density around 4 °C. This effect defines the only limitation of our method, for FIs made of pure water and having the lowest T_X. As dissolved salts suppress the anomalies in water and in particular decrease its temperature of maximum density[44], a better accuracy is obtained for FIs containing salt than for pure water. Literature data is available to calculate the uncertainty on T_X in the range 5–40 °C and for molalities up to 1 mol kg^{-1} (see Methods). The result is shown on Fig. 4d. For pure water, the calculation agrees well with the error from the fit for FI3. The calculated uncertainty increases at low temperatures, but it is significantly reduced for salt solutions. For instance, at 12 °C, we expect an uncertainty of 5.8 °C for pure water, and 2.5 °C for a 1 mol kg^{-1} NaCl solution. Molalities higher than 1 mol kg^{-1} would lead to an even lower uncertainty.

Discussion

Using FIs in quartz crystals, we have demonstrated the potential of our technique to uncover the value of T_X for a monophasic FI, with an initially unknown salt concentration. This provides an alternative approach to the laser-induced nucleation of bubbles in monophasic FI[32], with the following advantages: (i) the method does not risk damaging the inclusion, (ii) T_X values measured with Brillouin spectroscopy do not have to be corrected for surface tension effects[11,33], a correction that is available at present only for pure water. The application of the proposed technique to samples actually used in paleoclimate reconstruction (such as speleothems and evaporites) remains to be evaluated; this will be the subject of future work. If confirmed, the proposed paleothermometer would be particularly suitable for evaporitic deposits. Evaporites sediments in contact with water and air at the surface of Earth are able, by their rapid growth, to trap the fluids from which they precipitate (average precipitation rate in evaporitic basin is ca. 1 to 2 mm/year). The high salt concentrations in the trapped fluids are toxic for most organisms, preventing classical paleoclimatic reconstruction based on paleoecological and sedimentological analysis. The Brillouin paleothermometer, which becomes more accurate at higher salt concentrations, thus appears as a promising method to access seasonal temperature variations on Earth and sea surfaces.

Methods

Samples. We have studied one synthetic (FI1)[45] and three natural (FI2, FI3, and FI4 from the Mont Blanc massif in the Alps) FIs in pieces of quartz, cut perpendicular to the c axis (to avoid birefringence effects[46] in Raman spectroscopy), 300 and 200 μm thick, respectively, and polished on both sides. The FIs had a rounded shape, with a diameter around 4 to 8 μm (see Fig. 2a). They were observed with an upright microscope (Zeiss Axio Imager.Z2 Vario), equipped with a temperature stage (Linkam THMS 600) with 0.1 °C resolution, and a long-working distance ×100 objective (Mitutoyo Plan-Apo, N.A. 0.7). Values of T_h for each FI were obtained by direct observation of the bubble disappearance, with at least 5 independent determinations. For Brillouin and Raman calibration, reference NaCl solutions were prepared by dissolving anhydrous NaCl (Sigma, purity= 99.8%) in ultrapure water (Millipore, Direct Q3 UV), obtaining the desired molality by weighting.

Brillouin light scattering. More details about the setup and procedure are given in Ref. 47. We just give here a brief summary. For Brillouin scattering experiments, the light from a single longitudinal mode laser at $\lambda = 532$ nm (Coherent Verdi 6) was coupled to the microscope and focused to a 1 μm spot in the FI. The intensity was kept below 150 mW at the sample. The light backscattered into the objective was analysed with a 6-pass tandem Fabry-Perot interferometer (Sandercock TFP-1) to record its Brillouin spectrum; entrance and exit pinholes were 300 and 450 μm in diameter, respectively. A spectrum reached typically 300 counts at the Brillouin peak. The intensity as a function of the frequency shift Δf was fitted with the following function[48]:

$$I(\Delta f) = I_0\left[\frac{2 + \frac{\Delta f}{\sqrt{\Delta f_B^2 - \Gamma_B^2}}}{\left(\Delta f + \sqrt{\Delta f_B^2 - \Gamma_B^2}\right)^2 + \Gamma_B{}^2} + \frac{2 - \frac{\Delta f}{\sqrt{\Delta f_B^2 - \Gamma_B^2}}}{\left(\Delta f - \sqrt{\Delta f_B^2 - \Gamma_B^2}\right)^2 + \Gamma_B^2}\right], \quad (1)$$

convoluted with the instrumental response. I_0 is an intensity factor, and Δf_B and Γ_B are the Brillouin frequency and half-width, respectively. Based on repeated measurements on the same FI, performed for several FIs, and on the measurement of pure water from 0 to 120 °C along its liquid-vapour equilibrium, the total (1 standard deviation) uncertainty on Δf_B is 30 MHz. More details can be found in Ref. 47. The Brillouin shift measured in the backscattering geometry is given by:

$$\Delta f_B = \frac{2nw}{\lambda}, \quad (2)$$

where λ is the wavelength of light, and n and w are the refractive index and sound velocity of the liquid, respectively.

Raman spectroscopy. Raman spectra were also recorded with the same microscope setup from the backscattered light with a Raman spectrometer (Horiba Jobin-Yvon iHR 550, 300 lines mm^{-1} grating, 50 μm entrance slit). For FIs, the resolution of the setup was high enough to remove the quartz signal by a simple parabolic baseline correction. For solutions, a two-point linear baseline correction was sufficient. Spectra in the region of the OH stretching band were analysed as in Ref. 37, to give the total Cl^- molality.

Reference Brillouin shift. For pure water, Δf_B^{LVE} was calculated with equation (2) along the LVE using the IAPWS formulations for n[49] and w[50,51], valid over the whole range of temperatures of interest. For salty water, similarly to Raman, Δf_B^{LVE} depends essentially on the total Cl^- molality in the FI, with only a weak dependence on the cation. We used data for NaCl solutions. Equation (2) requires the sound

velocity w and refractive index n as a function of temperature T and molality m. Whereas w is available in the range 0–100 °C and 0–6 mol kg^{-1} (Ref. 39), n is available in the range 0–6 mol kg^{-1} but only at 20 °C (Ref. 38). To calculate n at other temperatures, we assumed the validity of the Gladstone-Dale relation (GDR): $n(T, m) = 1 + K\rho(T, m)$, where $\rho(T, m)$ is the solution density (available in the range 25–200 °C and 0–6 mol kg^{-1} (Ref. 52), and K is calculated from n and ρ at 20 °C and molality m (Ref. 38). GDR is known to be accurate for pure water[53]. Measurements on calibrated NaCl solutions in the range 20–60 °C and 0–2 mol kg^{-1} (Fig. 4b) confirmed that Δf_B^{LVE} calculated via the GDR is accurate. Moreover, based on the FI4 data (Fig. 4c), the calculation at $m = 1.20$ was also found to be reliable in the whole range 0–120°.

Calculation of the uncertainty on T_X. The finite uncertainty on the Brillouin shift, $\delta\Delta f_B = 30$ MHz (± 1 standard deviation)[47], translates into an uncertainty δT_X on T_X. It can be calculated as follows. For a salt solution with molality m, let $\Delta s(T_X, m)$ be the difference in slope between the isochore and the LVE that cross at T_X. To calculate the uncertainty on T_X, we treat $\Delta s(T_X, m)$ as a constant Δs, an assumption justified by the good results obtained with the linear fitting procedure described above. A measurement run generates N pairs of temperature and difference in shift $\left\{T_i,\ \Delta f_{B,i} - \Delta f_B^{LVE}(T_i, m)\right\}$ ($i = 1$ to N). This data set is fitted by the method of least squares with the linear function $\Delta s(T - T_X)$. T_X is thus obtained by minimizing the sum of squared residuals $\sum_{i=1}^{N}\left[\Delta f_{B,i} - \Delta f_B^{LVE}(T_i, m) - \Delta s\,(T_i - T_X)\right]^2$. It follows that:

$$T_X = \frac{1}{N}\sum_{i=1}^{N} T_i - \frac{1}{N\Delta s}\sum_{i=1}^{N}\left[\Delta f_{B,i} - \Delta f_B^{LVE}(T_i, m)\right]. \tag{3}$$

The dominant uncertainty is that on Δf_B, so that the uncertainty on T_X writes:

$$\delta T_X = \frac{\delta\Delta f_B}{\sqrt{N}\,\Delta s\,(T_X, m)}. \tag{4}$$

We have explained above how to compute $\Delta f_B^{LVE}(T, m)$. $\Delta f_B(T, m)$ along an isochore requires the knowledge of the sound velocity under pressure. It is available in a wide temperature range for pure water[50], but in a reduced range for NaCl solutions. We used sound velocity data for the ranges 5–40 °C, 0–100 MPa, and 0–1 mol kg^{-1} (Ref. 54). Combined with the density data[52] and the GDR (see above), we computed $\Delta s(T_X, m)$. The uncertainty calculated with equation (4) for a typical set of $N = 5$ Brillouin measurements is plotted on Fig. 4d.

References

1. Committee on Surface Temperature Reconstructions for the Last 2,000 Years, National Research Council. *Surface Temperature Reconstructions for the Last 2,000 Years* (The National Academies Press, Washington DC, 2006).
2. Yao, T. *et al.* δ^{18}O records from Tibetan ice cores reveal differences in climatic changes. *Ann. Glaciol.* **43,** 1–7 (2006).
3. Divine, D. *et al.* Thousand years of winter surface air temperature variations in Svalbard and northern Norway reconstructed from ice-core data. *Polar Res.* **30,** 7379 (2011).
4. Culleton, B. J., Kennett, D. J. & Jones, T. L. Oxygen isotope seasonality in a temperate estuarine shell midden: a case study from CA-ALA-17 on the San Francisco Bay, California. *J. Archaeol. Sci.* **36,** 1354–1363 (2009).
5. Lartaud, F. *et al.* A latitudinal gradient of seasonal temperature variation recorded in oyster shells from the coastal waters of France and The Netherlands. *Facies* **56,** 13–25 (2010).
6. Briffa, K. R., Osborn, T. J. & Schweingruber, F. H. Large-scale temperature inferences from tree rings: a review. *Glob. Planet. Change* **40,** 11–26 (2004).
7. D'Arrigo, R., Mashig, E., Frank, D., Jacoby, G. & Wilson, R. Reconstructed warm season temperatures for Nome, Seward Peninsula, Alaska. *Geophys. Res. Lett.* **31,** L09202 (2004).
8. D'Arrigo, R., Mashig, E., Frank, D., Wilson, R. & Jacoby, G. Temperature variability over the past millennium inferred from Northwestern Alaska tree rings. *Clim. Dyn.* **24,** 227–236 (2005).
9. Jiménez-Moreno, G., Fauquette, S. & Suc, J.-P. Miocene to Pliocene vegetation reconstruction and climate estimates in the Iberian Peninsula from pollen data. *Rev. Palaeobot. Palynol.* **162,** 403–415 (2010).
10. Lowenstein, T. K., Li, J. & Brown, C. B. Paleotemperatures from fluid inclusions in halite: method verification and a 100,000 year paleotemperature record, Death Valley, CA. *Chem. Geol.* **150,** 223–245 (1998).
11. Krüger, Y., Marti, D., Staub, R. H., Fleitmann, D. & Frenz, M. Liquid–vapour homogenisation of fluid inclusions in stalagmites: Evaluation of a new thermometer for palaeoclimate research. *Chem. Geol.* **289,** 39–47 (2011).
12. Zhao, Y.-J. *et al.* Late Eocene to early Oligocene quantitative paleotemperature record: Evidence from continental halite fluid inclusions. *Sci. Rep.* **4,** 5776 (2014).
13. Pujol, M., Marty, B., Burgess, R., Turner, G. & Philippot, P. Argon isotopic composition of Archaean atmosphere probes early Earth geodynamics. *Nature* **498,** 87–90 (2013).
14. Roedder, E. Liquid CO_2 inclusions in olivine bearing nodules and phenocrysts from basalts. *Am. Mineral.* **50,** 1746–1782 (1965).
15. Touret, J. L. Fluid regime in the lithosphere as indicated by fluid inclusions. *Mitteilungen Oesterreichischen Mineral. Ges.* **129,** 31–38 (1984).
16. Yardley, B. W. D. & Shmulovich, K. I. An introduction to crustal fluids in *Fluids in the Crust* (eds. Shmulovich, K. I., Yardley, B. W. D. & Gonchar, G. G.) Ch. 1, **1**–12 (Springer Netherlands, 1995).
17. Kramer, J. R. History of sea water. Constant temperature-pressure equilibrium models compared to liquid inclusion analyses. *Geochim. Cosmochim. Acta* **29,** 921–945 (1965).
18. Holser, W. T. Mineralogy of evaporites in *Reviews in Mineralogy*, Vol. **6** : Marine Minerals (ed. Burns, R. G.) Ch. **8**, 211–294 (Mineralogical Society of America, Chantilly, VA, 1979).

19. Holland, H. D. *The Chemical Evolution of the Atmosphere and Oceans* (Princeton University Press, 1984).
20. Lowenstein, T. K., Timofeeff, M. N., Brennan, S. T., Hardie, L. A. & Demicco, R. V. Oscillations in Phanerozoic seawater chemistry: Evidence from fluid inclusions. *Science* **294,** 1086–1088 (2001).
21. Horita, J., Zimmermann, H. & Holland, H. D. Chemical evolution of seawater during the Phanerozoic: Implications from the record of marine evaporites. *Geochim. Cosmochim. Acta* **66,** 3733–3756 (2002).
22. Van den Kerkhof, A. & Thiéry, R. Carbonic inclusions. *Lithos* **55,** 49–68 (2001).
23. Lowenstein, T. K., Spencer, R. J. & Pengxi, Z. Origin of ancient potash evaporites: Clues from the modern nonmarine Qaidam basin of Western China. *Science* **245,** 1090–1092 (1989).
24. Benison, K. C. Permian surface water temperatures from Nippewalla Group halite, Kansas. *Carbonate Evaporite* **10,** 245–251 (1995).
25. Roberts, S. M. & Spencer, R. J. Paleotemperatures preserved in fluid inclusions in halite. *Geochim. Cosmochim. Acta* **59,** 3929–3942 (1995).
26. Benison, K. C. & Goldstein, R. H. Permian paleoclimate data from fluid inclusions in halite. *Chem. Geol.* **154,** 113–132 (1999).
27. Satterfield, C. L., Lowenstein, T. K., Vreeland, R. H., Rosenzweig, W. D. & Powers, D. W. New evidence for 250 Ma age of halotolerant bacterium from a Permian salt crystal. *Geology* **33,** 265–268 (2005).
28. Rigaudier, T., Gardien, V., Martineau, F., Reverdy, G. & Lécuyer, C. Hydrogen and oxygen isotope reference materials for the analysis of water inclusions in halite. *Geostand. Geoanal. Res.* **36,** 51–59 (2012).
29. Newell, K. D. & Goldstein, R. H. A new technique for surface and shallow subsurface paleobarometry using fluid inclusions: an example from the Upper Ordovician Viola formation, Kansas, USA. *Chem. Geol.* **154,** 97–111 (1999).
30. Roedder, E. Interpretation and utilization of inclusion measurements - metastability in *Reviews in Mineralogy*, Vol. **12**: Fluid Inclusions (ed. Roedder, E.) Ch. **10**, 291–304 (Mineralogical Society of America, Chantilly, VA, 1984).
31. Tivey, M. K., Mills, R. A. & Teagle, D. A. Temperature and salinity of fluid inclusions in anhydrite as indicators of seawater entrainment and heating in the TAG active mound in *Proceedings-Ocean Drillling Program Scientific Results*, Vol. **158** (eds. Herzig, P. M. *et al.*) Ch. **14**, 179–192 (National Science Foundation, 1998).
32. Krüger, Y., Stoller, P., Rička, J. & Frenz, M. Femtosecond lasers in fluid-inclusion analysis: overcoming metastable phase states. *Eur. J. Mineral.* **19,** 693–706 (2007).
33. Marti, D., Krüger, Y., Fleitmann, D., Frenz, M. & Rička, J. The effect of surface tension on liquid–gas equilibria in isochoric systems and its application to fluid inclusions. *Fluid Phase Equilib.* **314,** 13–21 (2012).
34. Glavatskiy, K. S., Reguera, D. & Bedeaux, D. Effect of compressibility in bubble formation in closed systems. *J. Chem. Phys.* **138,** 204708 (2013).
35. Berne, B. J. & Pecora, R. *Dynamic Light Scattering: With Applications to Chemistry, Biology, and Physics* (Courier Corporation, 2000).
36. Fabre, C., Boiron, M.-C., Dubessy, J., Cathelineau, M. & Banks, D. A. Palaeofluid chemistry of a single fluid event: a bulk and *in-situ* multi-technique analysis (LIBS, Raman spectroscopy) of an Alpine fluid (Mont-Blanc). *Chem. Geol.* **182,** 249–264 (2002).
37. Dubessy, J., Lhomme, T., Boiron, M.-C. & Rull, F. Determination of chlorinity in aqueous fluids using Raman spectroscopy of the stretching band of water at room temperature: application to fluid inclusions. *Appl. Spectrosc.* **56,** 99–106 (2002).
38. Concentrative properties of aqueous solutions: density, refractive index, freezing point depression, and viscosity in *CRC Handbook of Chemistry and Physics* 95th edn (ed. Haynes, W..M.) Ch. **5**, 123–148 (CRC press, Boca Raton, Florida, 2014).
39. Millero, F. J., Vinokurova, F., Fernandez, M. & Hershey, J. P. PVT properties of concentrated electrolytes. VI. The speed of sound and apparent molal compressibilities of NaCl, Na_2SO_4, $MgCl_2$, and $MgSO_4$ solutions from 0 to 100oC. *J. Solut. Chem.* **16,** 269–284 (1987).
40. Frezzotti, M. L., Tecce, F. & Casagli, A. Raman spectroscopy for fluid inclusion analysis. *J. Geochem. Explor.* **112,** 1–20 (2012).
41. Baumgartner, M. & Bakker, R. J. Raman spectra of ice and salt hydrates in synthetic fluid inclusions. *Chem. Geol.* **275,** 58–66 (2010).
42. Pettke, T. *et al.* Recent developments in element concentration and isotope ratio analysis of individual fluid inclusions by laser ablation single and multiple collector ICP-MS. *Ore Geol. Rev.* **44,** 10–38 (2012).
43. Leisen, M., Dubessy, J., Boiron, M.-C. & Lach, P. Improvement of the determination of element concentrations in quartz-hosted fluid inclusions by LA-ICP-MS and Pitzer thermodynamic modeling of ice melting temperature. *Geochim. Cosmochim. Acta* **90,** 110–125 (2012).
44. Mironenko, M. V., Boitnott, G. E., Grant, S. A. & Sletten, R. S. Experimental determination of the volumetric properties of NaCl solutions to 253 K. *J. Phys. Chem. B* **105,** 9909–9912 (2001).
45. Shmulovich, K. I., Mercury, L., Thiéry, R., Ramboz, C. & El Mekki, M. Experimental superheating of water and aqueous solutions. *Geochim. Cosmochim. Acta* **73,** 2457–2470 (2009).
46. Baumgartner, M. & Bakker, R. J. Raman spectroscopy of pure H_2O and NaCl-H_2O containing synthetic fluid inclusions in quartz—a study of polarization effects. *Mineral. Petrol.* **95,** 1–15 (2009).
47. Pallares, G. *et al.* Anomalies in bulk supercooled water at negative pressure. *Proc. Natl. Acad. Sci. USA* **111,** 7936–7941 (2014).
48. Magazu, S. *et al.* Relaxation process in deeply supercooled water by Mandelstam-Brillouin scattering. *J. Phys. Chem.* **93,** 942–947 (1989).
49. The International Association for the Properties of Water and Steam. Release on the refractive index of ordinary water substance as a function of wavelength, temperature and pressure (1997). http://www.iapws.org/relguide/rindex.pdf, Date of access: 15/01/2015.
50. The International Association for the Properties of Water and Steam. Revised release on the IAPWS formulation 1995 for the thermodynamic properties of ordinary water substance for general and scientific use (2014). http://www.iapws.org/relguide/IAPWS95-2014.pdf, Date of access: 15/01/2015.
51. The International Association for the Properties of Water and Steam. Revised supplementary release on saturation properties of ordinary water substance (1992). http:// www.iapws.org/relguide/supsat.pdf, Date of access: 15/01/2015.
52. Al Ghafri, S., Maitland, G. C. & Trusler, J. P. M. Densities of aqueous $MgCl_2$(aq), $CaCl_2$(aq), KI(aq), NaCl(aq), KCl(aq), $AlCl_3$(aq), and (0.964 NaCl + 0.136 KCl)(aq) at temperatures between 283 and 472 K, pressures up to 68.5 MPa, and molalities up to 6 mol kg^{-1}. *J. Chem. Eng. Data* **57,** 1288–1304 (2012).
53. Arvengas, A., Davitt, K. & Caupin, F. Fiber optic probe hydrophone for the study of acoustic cavitation in water. *Rev. Sci. Instrum.* **82,** 034904 (2011).
54. Chen, C.-T., Chen, L.-S. & Millero, F. J. Speed of sound in NaCl, $MgCl_2$, Na_2SO_4, and $MgSO_4$ aqueous solutions as functions of concentration, temperature, and pressure. *J. Acoust. Soc. Am.* **63,** 1795–1800 (1978).

Acknowledgements

We thank Abraham D. Stroock for proof-reading the manuscript. F.C. acknowledges funding by the European Research Council under the European Community's FP7 Grant Agreement 240113, and by the Agence Nationale de la Recherche Grant 09-BLAN-0404-01. This study was financially supported by the

Agence Nationale de la Recherche, project no. ANR-08-BLAN-0303-01 "Erosion and Relief Development in the Western Alps".

Author Contributions

F.C. and V.G. conceived the project. M.E.M.A., C.S.P.T. and G.P. carried out the experimental work. M.E.M.A., C.S.P.T., G.P. and F.C. analysed the data. F.C. and V.G. wrote the manuscript with input and advice from M.E.M.A., C.S.P.T. and G.P.

Additional Information

Competing financial interests: The authors declare no competing financial interests.

How to cite this article: El Mekki-Azouzi, M. *et al.* Brillouin spectroscopy of fluid inclusions proposed as a paleothermometer for subsurface rocks. *Sci. Rep.* **5**, 13168; doi: 10.1038/srep13168 (2015).